JOURNAL OF GEOPHYSICAL RESEARCH, VOL. 115, B07211, doi:10.1029/2009JB007118, 2010

Constraints on compaction rate and equilibrium in the pressure solution creep of quartz aggregates and fractures: Controls of aqueous concentration

Joshua Taron[1,2] and Derek Elsworth[1]

Received 11 November 2009; revised 26 February 2010; accepted 5 March 2010; published 31 July 2010.

[1] A relationship is developed to examine dissolution precipitation creep in crustal rocks with implicit coupling of the dissolution-diffusion-precipitation system and without requiring the iterative solution of a linear equation system. Implicit control is maintained over aqueous silica concentrations within hydrated solid contacts and in open pore space. For arbitrary conditions of temperature, pressure, and mechanical stress, the simple equation system conforms to a polynomial solution for aqueous concentrations set within a small iterative compaction scheme. Equilibrium (long-term) pressure solution compaction, previously ill constrained, is explored with two alternate methods: (1) a modified form of critical stress and (2) rate-controlled growth of diffusion limiting cement at the periphery of solid contacts. Predictions are compared to previous experimental results that allow compaction equilibrium to be achieved. Only the modified critical stress is capable of reproducing these results. In this case the agreement is strong across a range of conditions (400°C–500°C, 20–150 MPa, and 3–120 μm mean particle diameter). Compaction rates are overestimated in very early times in a manner suggesting the importance of plastic flow during this period. Predictions are also compared to concentration independent simplifications at general conditions of 350°C and 50 MPa. Compared to the implicit coupling, these methods represent the mean behavior, slightly underestimating rates in dissolution control and slightly overestimating in diffusion control. Aqueous concentration is influential in either regime. The solution is applicable to open and closed systems, is extended to systems with boundary influx, and may be applied to granular media or fractures, differing only in the method defining evolving contact geometry.

Citation: Taron, J., and D. Elsworth (2010), Constraints on compaction rate and equilibrium in the pressure solution creep of quartz aggregates and fractures: Controls of aqueous concentration, *J. Geophys. Res.*, *115*, B07211, doi:10.1029/2009JB007118.

1. Introduction

[2] Intergranular pressure solution is an important chemo-mechanical creep process in crustal rocks. In rock fractures and porous aggregates, mechanical load is concentrated at a finite number of contact points, and if these locations are hydrated by a thin water film [*Revil*, 2001; *Rutter*, 1976; 1983; *Weyl*, 1959] and/or by a dynamic island-channel network [*Lehner*, 1995; *Raj*, 1982; *Schutjens and Spiers*, 1999], then the activity of stressed minerals in contact with the fluid is elevated. Under these conditions, enhanced dissolution and supersaturation within the contact are thermodynamically favored [*De Boer*, 1977; *Paterson*, 1973]. A chemical potential gradient may then evolve for the diffusive migration of aqueous species across the grain boundary for eventual precipitation to hydrostatically stressed pore walls. Combined, these serial processes lead to porosity and permeability reduction by compaction of the solid and infilling of voids, providing a potentially important contribution to diagenesis and fault healing [*Sleep*, 1995; *Tada and Siever*, 1989; *Yasuhara et al.*, 2005] and the evolution of engineered, fractured reservoirs [cf. *Taron and Elsworth*, 2009].

[3] Despite many previous attempts to model the serial pressure solution mechanism, a fully predictive model remains elusive. Several schemes have been proposed to extend predictive capability beyond a given experiment [*Dewers and Ortoleva*, 1990b; *Gunderson et al.*, 2002; *He et al.*, 2002; *Lehner*, 1995; *Renard et al.*, 1997; *Renard et al.*, 1999; *Revil*, 1999; 2001; *Yasuhara et al.*, 2003]. In most cases it is necessary to assume a priori whether diffusion or dissolution is the rate-limiting step, or to allow a smooth transition between these processes. *Gunderson et al.* [2002] presented a fully mechanistic model with implicit coupling between dissolution, diffusion, and precipitation. *Yasuhara et al.* [2003] introduced an approach for the implicit coupling that did not require an iterative solution of a larger linear equation system, but in doing so, some control was lost over the

[1]College of Earth and Mineral Sciences and Center for Geomechanics, Geofluids, and Geohazards, Penn State University, University Park, Pennsylvania, USA.
[2]Now at Helmholtz Center for Environmental Research (UFZ), Department of Environmental Informatics, Leipzig, Germany.

0148-0227/10/2009JB007118

chemical potential gradient for diffusion, leading to overestimation of interfacial concentrations and diffusion rates.

[4] In all cases the mechanism leading to the cessation of pressure solution at some final, nonzero value of porosity remains poorly constrained [*Revil et al.*, 2006; *van Noort et al.*, 2008b]. Other models of interest include the cementation model of *Walderhaug* [1996] and the ("plastic") total expended energy model of *Stephenson et al.* [1992]. Each of these studies has provided valuable insights into pressure solution theory that contribute strongly to the mechanism proposed herein.

[5] Following the approach of *Yasuhara et al.* [2003], a simple finite element equation system is proposed to examine the three serial processes of pressure solution. It is shown that with a slightly fuller thermodynamic treatment, complete control can be maintained on interfacial and pore fluid aqueous concentrations without the iterative solution of a linear equation system. The solution is applicable to open and closed systems and to granular aggregates or fractures. Sections 3–4 present the derivation of this model. Final compaction magnitudes are examined utilizing the concept of "critical stress," first proposed by *Stephenson et al.* [1992], and grain periphery healing (as neck growth) as discussed by, for example, *Visser* [1999] and *van Noort et al.* [2008b] by allowing rate-dependent deposition of supporting cement around grain boundaries. Results are compared to experimental observations [*Niemeijer et al.*, 2002; *van Noort et al.*, 2008a] on granular quartz that allow compaction to achieve a final equilibrium.

2. Note on Stress Corrosion

[6] Both pressure solution and stress corrosion [*Atkinson*, 1984; *Dove*, 1995] (the chemical erosion of microcrack tip strength) have been shown to exhibit behavior in agreement with the rate and activation energy of chemical dissolution [*Dewers and Hajash*, 1995; *Schutjens*, 1991], and so it is often difficult to distinguish the contribution of each process through macroscopic observations. At higher temperatures and pressures (>400°C and >50 MPa), pressure solution may generally dominate behavior [*Niemeijer et al.*, 2002; *Tenthorey and Cox*, 2006]. At lower temperatures (150°C–250°C and >30 MPa), however, results are mixed and conflicting (see detailed discussion in the study of *Chester et al.* [2007]). A common consensus [e.g., *Schutjens*, 1991] is that there exists a transitional period (~150°C–200°C) where pressure solution becomes an active process. Below this value, only subcritical crack growth is thermodynamically favored, and above it, pressure solution eventually dominates [*Chester et al.*, 2007; *Dewers and Hajash*, 1995; *Schutjens*, 1991]. This paper focuses on the detailed mechanism of pressure solution and examines conditions well in excess of the suspected transitional stage. See *Yasuhara and Elsworth* [2008] for a recent attempt to combine both processes.

3. Thermodynamic Potential and the Rate Equations

[7] This section presents the fundamental thermodynamic, kinetic, and diffusive relationships for our composite model. The form is presented as briefly as possible to avoid redundancy with available literature. The novelty of this section rests in the use of equation (10) rather than the usual approximation of equation (11) to represent the rate of dissolution within stressed granular contacts, thus, maintaining dependence on aqueous chemical concentrations. Fick's law for diffusion is solved for boundaries of constant flux within intergranular contacts, although alternate boundary conditions produce only slightly different results. All geometric parameters are derived in terms of a representative elementary volume (REV) for physical clarity. The resulting quantities are relative, such that the initial volume, V_0, assigned to the REV is arbitrary.

3.1. Contact Area

[8] The response of both compacting fractures and granular aggregates may be accommodated through a common consideration of evolving contact area. In bare fractures, two opposing fracture planes are held apart by deformable asperities, where effective stress concentrates as a function of real contact area. The contact area ratio is the relationship between real area of contact (summed over all contacting asperities) to total square area (over which a load is applied), $R_c = A_c/A_T$. In granular aggregates, although typically referred to as contiguity, φ, the meaning is transferrable, and refers to the fraction of total granular surface area that is in contact ($(1 - \varphi)$ is wetness). By continuity of stress, the load supported at contacts is $\sigma_a = \sigma'/R_c = \sigma'/\varphi$, where σ' is effective stress ($\sigma' = \sigma - p$), with stress positive in compression. Holding with previous terminology, σ_a is the disjoining stress, although here σ_a is defined as an effective stress.

3.2. Grain Boundary Structure

[9] The geometric structure of evolving grain boundaries remains a subject of debate. *Revil* [2001] suggests that repulsive steric forces are sufficient within grain boundaries to sustain a thin film thickness of several nanometers, and the recent quartz indenter experiments of *Gratier et al.* [2009] observed behavior consistent with a thin film thickness of 2–10 nm. *Karcz et al.* [2008] conducted halite indenter experiments and visually observed dynamic changes to the grain boundary, where R_c at a single contact may vary from 20% to 70% (for $\sigma' \approx$ 7–30 MPa) and evolves throughout the course of a single experiment. Similar evolving contact fraction was observed in the halite experiments of *de Meer et al.* [2005]. *Karcz et al.* [2008] suggests that this behavior can be explained by a combination of pressure solution, plastic flow, and undercutting around the contact periphery. It is unclear how such plastic flow behavior will translate to silica, exhibiting a much higher compressive strength, but it will most certainly play some role in the compaction process. Additionally, there is some debate surrounding the thermodynamic stability of so-called island and channel models [*Lehner*, 1995; *Raj*, 1982; *Schutjens and Spiers*, 1999; *van Noort et al.*, 2008b], although remnants of such a structure have been observed visually in the study, for example, by *Cox and Paterson* [1991] for quartz materials. It is reasonable to suspect that all of these behaviors are real and may be present and that the ability of a given pressure solution model to reproduce laboratory data stems from its ability to represent mean behavior, in all cases signified by the reaction rate of stressed silica.

[10] In island and channel models, *Schutjens and Spiers* [1999] (and others) introduce the parameter α, representing

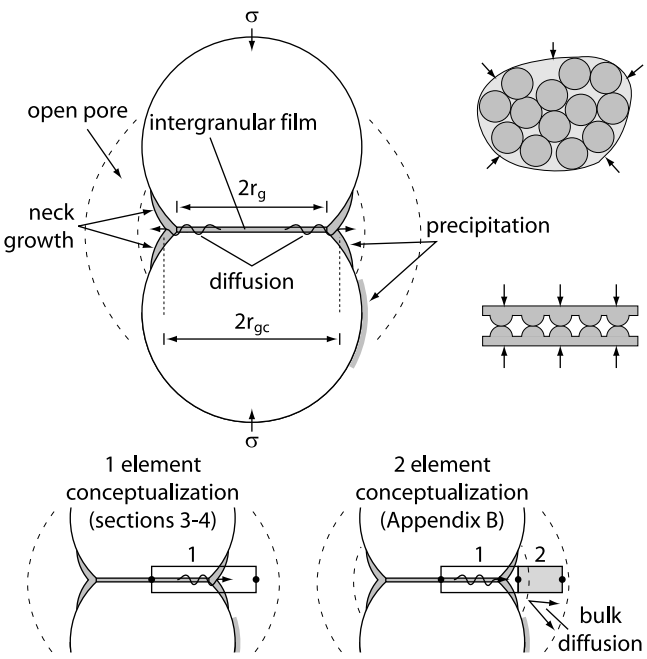

Figure 1. Conceptualization of the chemical compaction process, porous media, and fractures.

the fraction of the grain boundary occupied by solid contacting islands. A complete island-channel model is not considered here, but some the effects of a nonuniform granular contact may be taken into account by considering generally how such a structure modifies contact area and stress concentration.

[11] While α is poorly constrained and the processes leading to its evolution complex, the laboratory results of *Karcz et al.* [2008] and *Cox and Paterson* [1991] indicate that the *most* unreasonable assumption is that intergranular contacts ever exhibit $\alpha = 1$ (even at very high stress and temperature [*Cox and Paterson*, 1991]). Our modeling suggests α in the range 0.3–0.4 for the variable conditions examined below, which is in reasonable agreement with the discussion above. In all results presented here, α is assumed to be a constant with a value of 0.30. Setting $\alpha = 1$ in all equations that follow would negate its effect.

3.3. Chemical Potential

[12] As derived by many previous authors, the driving force for pressure solution is represented as the chemical potential difference between a stressed contact and a hydrostatically stressed open pore [*De Boer*, 1977; *Heidug*, 1995; *Kamb*, 1959; *Lehner*, 1995; *Paterson*, 1973]

$$\Delta\mu = \frac{\sigma_a V_m}{\alpha} + \Delta f - U_S, \tag{1}$$

where the surface energy term [*Heidug*, 1995],

$$U_S = 2H\gamma_G, \tag{2}$$

V_m is the molar volume, Δf is the molar Helmholtz free energy difference, and surface energy includes the local solid/fluid interface curvature, H, and the Gibbs surface energy, γ_G (numerically equivalent to the surface tension [*Heidug*, 1991]). Helmholtz energy includes contribution from elastic strain energy and dislocation energy, $\Delta f = U_E + U_D$. The molar elastic strain energy is given approximately by

$$U_E \approx V_m \frac{\sigma_a^2}{2E_m\alpha^2} \tag{3}$$

[*De Boer*, 1977; *Paterson*, 1973], where E_m is Young's modulus. For reasonable values of mineral compliance, the contribution from strain energy is strongly overshadowed by P-V work (first term in equation (1)) [see also *Paterson*, 1973], and some numerical estimations of the contribution from elastic strain, dislocation, and the surface energy term are discussed in the study of, for example, *Renard et al.* [1999].

3.4. Rate Equation Formalism

[13] A general geometric idealization of the pressure solution process is provided in Figure 1. Dissolution/precipitation of silica in the intergranular film and open pore space follows the simple elementary reaction,

$$SiO_{2(s)} + 2H_2O \Leftrightarrow H_4SiO_{4(aq)}. \tag{4}$$

A more accurate reaction mechanism would include the precipitation/dissolution of a quartz/amorphous silica system. This first analysis utilizes a composite reaction system, where reaction rates represent the bulk behavior of all silica compounds. Hydrostatic solubility of silica is extracted directly from the study of *Rimstidt and Barnes* [1980], while a slightly higher (compared to their work) dissolution rate constant is adopted; 5.04×10^{-14} mol m^{-2} s^{-1} at 25°C, with an activation energy of 67.4 kJ/mol. A comprehensive review of literature reaction rates for quartz is given by *Bandstra et al.* [2008].

[14] The equilibrium constant for this reaction is

$$K_{eq} = \frac{a_{H_4SiO_4}}{a_{SiO_2} a_{H_2O}}. \tag{5}$$

At chemical equilibrium in the unstressed pore space, the activities of both water and unstressed solid silica are assumed unity, so that the equilibrium constant may be simplified and related to the equilibrium solubility as

$$K_{eq}^h = a_{H_4SiO_4} = \gamma^h C_{eq}^h, \tag{6}$$

where superscript, h, refers to the hydrostatic state, γ is the activity coefficient, and C_{eq}^h is the solubility of aqueous silica. For equation (6) to hold, solubility requires units of molar fraction. In all remaining equations, concentrations and activities appear in ratios, thus, allowing SI units of concentration (mol · m^{-3}). Utilizing the definition of chemical potential, $\mu = \mu^* + RT \ln(a)$, the relationship between hydrostatic solubility and the solubility under elevated stress is

$$\gamma^\sigma C_{eq}^\sigma = \gamma^h C_{eq}^h \exp\left(\frac{\Delta\mu}{RT}\right) \tag{7}$$

[*Paterson*, 1973], where the superscript, σ, refers to a state of nonhydrostatic stress (h is hydrostatic), and the last term represents the activity of solid silica under stress

$$a_{SiO_2} = \exp\left(\frac{\Delta\mu}{RT}\right) \tag{8}$$

[*De Boer*, 1977; *Dewers and Ortoleva*, 1990a; *Shimizu*, 1995]. This relationship conveys the stress dependence of solid chemical potential (for the stressed solid in equilibrium with its fluid), visited in solubility (equation (7)) and reaction rate (equation (9)). When no excess chemical potential exists for the solid (in the hydrostatic pore space), solid activity approaches unity. Following from equation (9), simplifications of equation (8) produce the most common representation of stress-enhanced reaction rate, that of equation (11). See *Dewers and Ortoleva* [1990a] and *De Boer* [1977] for more detailed derivations. The general form for reaction rate is (positive for dissolution)

$$\dot{m}^{rx}\left[\text{mol s}^{-1}\right] = k^{+}\alpha A^{rx} a_{SiO_2}\left(1 - \frac{a_{H_4SiO_2}}{K^{h}_{eq} a_{SiO_2}}\right) \tag{9}$$

[*Dewers and Ortoleva*, 1990a; *Rimstidt and Barnes*, 1980; *Shimizu*, 1995], where k^{+} [mol m^{-2} s^{-1}] = $K^{h}_{eq}k^{-}$ is the forward (dissolution) rate constant and A^{rx} is the reaction area (modified by fractional area of the contact, α). Substituting equation (8) into (7) and the result into equation (9) (second bracketed term) and assuming that activity coefficients can be neglected as unity produces the rate equation for mass flux within the intergranular (subscript i) contacts,

$$\dot{m}^{rx}_{i} = k^{+}\alpha A^{rx}_{i} a_{SiO_2}\left(1 - \frac{\tilde{C}_i}{C^{\sigma}_{eq}}\right), \tag{10}$$

where $\tilde{C}_i$ is the mean current concentration of aqueous silica in the intergranular fluid film, A^{rx}_{i} is the total (nominal) geometric surface area within (REV) intergranular contacts. Referencing equations (7) and (8), $C^{\sigma}_{eq} = a_{SiO_2} C^{h}_{eq}$. In practice, it is difficult to produce an analytical relationship capable of tracking time-dependent aqueous concentrations, and so, two approximations are enacted. The first assumes a_{SiO_2} = $\exp(\Delta\mu/RT) \approx \Delta\mu/RT + 1$. Second, although the thermodynamic derivations follow an alternate approach (see, for example, *Lehner* [1995]), the dependence on $\tilde{C}_i$ is relieved by the assumption $\tilde{C}_i/C^{h}_{eq} = 1$. These substitutions produce

$$\dot{m}^{rx}_{i} \approx k^{+}\alpha A^{rx}_{i}\frac{\Delta\mu}{RT}, \tag{11}$$

which is the widely used rate equation for dissolution within a stressed contact. Substituting for $\sigma_a = \sigma'(A_T/A^{rx}_{i})$ and approximating Δf by equation (3),

$$\dot{m}^{rx}_{i} = \frac{k^{+}V_m}{RT}\left(\sigma' A_T + \frac{(\sigma' A_T)^2}{2\alpha A^{rx}_{i} E_m} - \frac{U_S}{\alpha A^{rx}_{i}}\right), \tag{12}$$

which shows that all contact area, A^{rx}_{i}, and roughness, α, dependence is contained within the strain energy and surface energy terms. Therefore, if U_S is small relative to $\sigma_a V_m + \Delta f$, the dissolution rate at granular contacts will not change as a function of continued interpenetration. This problem, which, for a thin film model, excludes the possibility of compaction equilibrium for reasonable values of Δf and U_S, is discussed further in section 5. The mechanism presented below utilizes equation (10) directly rather than equation (11), retaining the dependence on evolving concentrations.

[15] Reaction rate in the hydrostatic pore space (subscript, p) can be extracted from equation (10) by allowing $a_{SiO2} = 1$ and removing α,

$$\dot{m}^{rx}_{p} = k^{+}A^{rx}_{p}\left(1 - \frac{\tilde{C}_p}{C^{h}_{eq}}\right), \tag{13}$$

where A^{rx}_{p} is total (nominal) available surface area within the pore space, $\tilde{C}_p$ is the mean current concentration at the periphery of the grain (the pore space), and, as above, the result is positive for dissolution. In the full iterative scheme, both A^{rx}_{p} and A^{rx}_{i} evolve in time with the progression of asperity or grain surface interpenetration. They represent total reactive areas within the REV.

3.5. Intergranular Diffusion

[16] Molecular diffusion of solute mass occurs over a chemical potential gradient, represented here by concentration. Under constant material flux, F, the cylindrical diffusion/conduction equation takes the form

$$F = -D_f\frac{1}{r}\frac{d}{dr}\left(r\frac{dC}{dr}\right) \tag{14}$$

[*Carslaw and Jaeger*, 1959, equation 7.14] (Poisson's equation) within an infinite circular cylinder of radius, r, and for the molecular diffusivity, D_f. The solution for radial distribution of concentration within the cylinder (from $r = 0$ to $r = a$) is

$$C(r) = C_a + \frac{F}{4D_f}\left(a^2 - r^2\right). \tag{15}$$

[*Carslaw and Jaeger*, 1959, equation 7.17]; equation (15) admits a quadratic concentration profile from the center, $r = 0$, to periphery, $r = a$. Integrating this relationship from $r = 0$ to $r = a$ and then averaging the (resulting) concentration across the surface (πa^2) yields, in terms of the mean concentrations,

$$F = 8D_f\left(\tilde{C}_i - \tilde{C}_p\right) \tag{16}$$

[*Lehner*, 1995] for the flux per unit length of the cylinder. Equation (16) is modified further by *Lehner* [1995] in a manner that removes the direct dependence on transient concentration (see also *Rutter* [1976]). As we will use this equation directly, no further modification is required. Alternate boundary conditions (such as constant concentration at grain boundary center) produce a slightly different geometric factor.

[17] Equation (16) represents diffusive flux at a single granular contact while equations (10) and (13) were derived for total flux in the REV; agreement requires multiplication

by the number of granular contacts within the REV, $A_i^{rx}/2a_g$ (reduced by 2 surfaces per contact), to give

$$\dot{m}^{diff}\left[\text{mol s}^{-1}\right] = 8D_f\omega\left(\tilde{C}_i - \tilde{C}_p\right)\cdot\frac{A_i^{rx}}{2a_g}, \tag{17}$$

where multiplication by the grain boundary width, ω, reduces the unit length cylinder to the thickness of the intergranular film and a_g is the current mean contact radius (of each contact).

[18] The behavior of intergranular molecular diffusion is discussed in detail by, for example, *Revil* [2001]. Molecular diffusivity, D_f, is given by the Stokes-Einstein equation,

$$D_f = \frac{kT}{6\pi\eta\delta}, \tag{18}$$

for the Boltzmann constant, $k = 1.38 \times 10^{-23}$ m^3 Pa s^{-1}, water viscosity, η, at temperature, T, and with the diameter of a molecule of hydrated silica, $\delta \approx 0.5$ nm [*Renard et al.*, 1999]. Note that in experimental studies, it is difficult or impossible to measure D_f directly, but rather, it is the product $D_f\omega$ that is measured.

4. Composite Mass Balance

[19] Utilizing equations (10), (13), and (17), and referencing Figure 1 (single element formulation), mass balances on the intergranular space and the open pore, respectively, produce the relationships

$$\dot{C}_i V_i = k^+\alpha A_i^{rx} a_{SiO_2}\left(1 - \frac{\tilde{C}_i}{a_{SiO_2}C_{eq}^h}\right) - D\left(\tilde{C}_i - \tilde{C}_p\right) \tag{19}$$

$$\dot{C}_p V_p = k^+ A_p^{rx}\left(1 - \frac{\tilde{C}_p}{C_{eq}^h}\right) + D\left(\tilde{C}_i - \tilde{C}_p\right). \tag{20}$$

Here $V_i = \omega A_i^{rx}/2$ is total REV volume within the grain contacts, $V_p = \phi V$ is total REV pore volume, the overdot refers to the time rate of change of the given quantity, and

$$D = 8D_f\omega\cdot\left(\frac{A_i^{rx}}{2a_g}\right). \tag{21}$$

Combining equations (19) and (20) produces the linear system (by redistributing source terms),

$$\begin{Bmatrix} k^+\alpha A_i^{rx} a_{SiO_2} \\ k^+ A_p^{rx} \end{Bmatrix} = \begin{bmatrix} V_i & 0 \\ 0 & V_p \end{bmatrix}\begin{Bmatrix} \dot{C}_i \\ \dot{C}_p \end{Bmatrix} + D\begin{bmatrix} \left(\frac{k^+\alpha A_i^{rx}}{DC_{eq}^h} + 1\right) & -1 \\ -1 & \left(\frac{k^+ A_p^{rx}}{DC_{eq}^h} + 1\right) \end{bmatrix}\begin{Bmatrix} C_i \\ C_p \end{Bmatrix}. \tag{22}$$

Equation (22) mimics the general finite element formalism, $\mathbf{q} = \mathbf{V}\dot{\mathbf{C}} + \mathbf{K}\mathbf{C}$, which admits the implicit solution, $\mathbf{C}_{t+\Delta t} = \left[\mathbf{K} + \frac{1}{\Delta t}\mathbf{V}\right]^{-1}\left[\mathbf{q} + \frac{1}{\Delta t}\mathbf{V}\mathbf{C}_t\right]$. Performing the multiplication yields,

$$\begin{Bmatrix} C_i \\ C_p \end{Bmatrix}_{t+\Delta t} = D\begin{bmatrix} \left(\frac{k^+\alpha A_i^{rx}}{DC_{eq}^h} + 1\right) + \frac{V_i}{\Delta t} & -1 \\ -1 & \left(\frac{k^+ A_p^{rx}}{DC_{eq}^h} + 1\right) + \frac{V_p}{\Delta t} \end{bmatrix}_t^{-1} \times \begin{Bmatrix} k^+\alpha A_i^{rx} a_{SiO_2} + \frac{V_i C_i}{\Delta t} \\ k^+ A_p^{rx} + \frac{V_p C_p}{\Delta t} \end{Bmatrix}_t \tag{23}$$

Because this solution is fully implicit in time, the mass of silica removed from intergranular contacts over a single time step is not directly recovered from equation (23) (as would be the case in an explicit solution). This quantity, which is necessary to obtain the rate of grain convergence over a time step, may be obtained from equation (22) in a way that maintains the implicit accuracy. Rearranging the finite element solution: $\mathbf{q} - \mathbf{K}\mathbf{C}_{t+\Delta t} = \frac{1}{\Delta t}\mathbf{V}[\mathbf{C}_{t+\Delta t} - \mathbf{C}_t]$. Performing the matrix multiplication and solving for the complete source term, $\dot{m}_i^{rx} = k^+\alpha A_i^{rx} a_{SiO_2}(1 - C_i/C_{eq}^{\sigma})$, shows that, once the concentrations at time $t + \Delta t$ from equation (23) are obtained, the mass removal resulting in grain convergence over that time step is

$$\Delta m_i^{SiO_2} = \dot{m}_i\Delta t = V_i\left(C_i^{t+\Delta t} - C_i^t\right) + D\left(C_i^{t+\Delta t} - C_p^{t+\Delta t}\right)\Delta t \tag{24}$$

([moles SiO_2], positive for grain convergent dissolution). And likewise, for dissolution/precipitation in the pore space (negative for moles precipitated in the pore),

$$\Delta m_p^{SiO_2} = \dot{m}_p\Delta t = V_p\left(C_p^{t+\Delta t} - C_p^t\right) - D\left(C_i^{t+\Delta t} - C_p^{t+\Delta t}\right)\Delta t. \tag{25}$$

For this single element solution, these results may also be inferred by revisiting equations (19)–(20) with $\mathbf{C}_{t+\Delta t}$ given by equation (23). For the two element solution presented in Appendix B, it is necessary to perform this matrix manipulation to obtain equivalent forms of equations (24) and (25). The complete calculation sequence is shown in Figure 2. The implicit solution is unconditionally stable. However, all geometric identities (section 4.2) are updated incrementally in time, and so, a reasonably small time step is required. Time step sensitivity analyses were conducted to ensure accuracy, with Δt controlled adaptively and defined to maintain grain convergence rate beneath a prespecified tolerance.

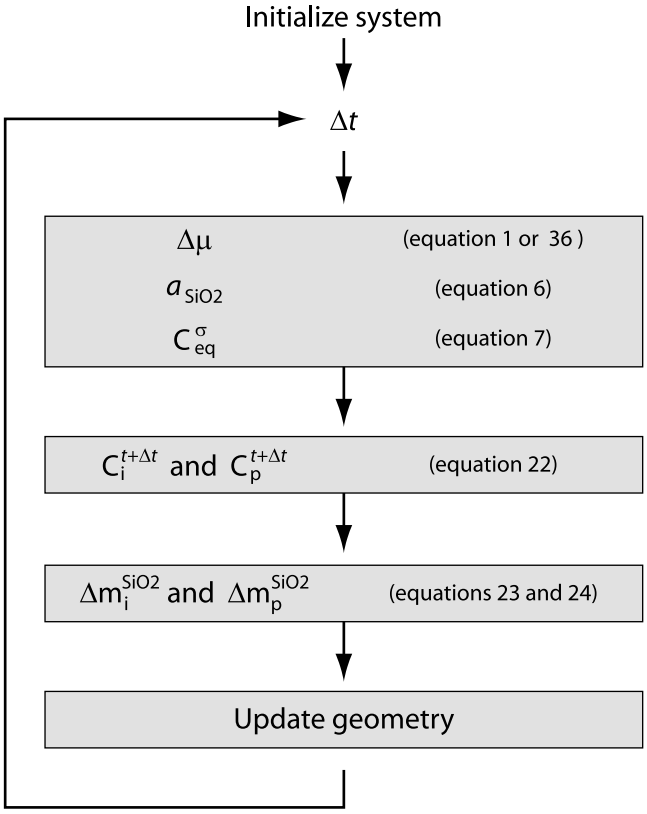

Figure 2. Calculation sequence for composite model (single element solution, section 4).

4.1. Systems With Boundary Influx

[20] Assuming a steady state influx of boundary water, Q_{ss}, and revisiting the pore fluid mass balance yields a flowing system form of equation (20),

$$\dot{C}_p V_p = k^+ A_p^{rx}\left(1 - \frac{\tilde{C}_p}{C_{eq}^h}\right) + D\left(\tilde{C}_i - \tilde{C}_p\right) - Q_{ss}\tilde{C}_p. \qquad (26)$$

Combining equations (19) and (26) yields the open system (analogous with equation (22)),

$$\begin{Bmatrix} k^+\alpha A_i^{rx} a_{SiO_2} \\ k^+ A_p^{rx} \end{Bmatrix} = \begin{bmatrix} V_i & 0 \\ 0 & V_p \end{bmatrix} \begin{Bmatrix} C_i \\ C_p \end{Bmatrix} + D\begin{bmatrix} \left(\frac{k^+\alpha A_i^{rx}}{DC_{eq}^h} + 1\right) & -1 \\ -1 & \left(\frac{k^+ A_p^{rx}}{DC_{eq}^h} + \frac{Q_{ss}}{D} + 1\right) \end{bmatrix} \cdot \begin{Bmatrix} C_i \\ C_p \end{Bmatrix}. \qquad (27)$$

The implicit solution to this system is obtained by following the same procedure as in the previous section. There are many environments, such as open fracture systems, where boundary influx may deplete pore fluid concentrations of dissolved silica and thereby speed the rate of pressure solution convergence. Such environments would require the use of equation (27) rather than equation (22).

4.2. System Geometry

[21] The change in mechanical aperture of the fracture (mean separation between contacting fracture surfaces) over a time step is obtained from

$$\Delta b_m = \frac{\Delta m_i^{SiO_2} V_m}{2A_{rx}^i}. \qquad (28)$$

This differs from the so-called hydraulic aperture (b_h), which relates to fracture permeability as $k = b_h^2/12$ (cubic law) and includes the effects of fracture roughness on fluid flow. For such fracture systems, A_i^{rx} may be calculated from an appropriate contact theory [cf. *Brown and Scholz*, 1986] or through direct comparison of fracture profile data [*Yasuhara et al.*, 2004].

[22] For granular systems, additional considerations are required. For isotropic compaction, the strained volume to reference volume ratio is (referencing Figure 3)

$$\frac{V}{V_0} = \left(\frac{r_i - h}{r_i}\right)^3, \qquad (29)$$

positive for compaction and where h is cumulative granular interpenetration, r_i is the initial mean particle radius, and V_0 and V are the initial and current REV volumes, respectively. Rearrangement produces the relationship for finite volume strain

$$\varepsilon_v \equiv \frac{V_0 - V}{V_0} = 1 - \left(1 - \frac{h}{r_i}\right)^3 \qquad (30)$$

[*Jaeger et al.*, 2007]. Cumulative interpenetration, h, is calculated incrementally in time, beginning at 0 and incrementing by $\Delta h = (\Delta m_i^{SiO_2} V_m)/A_i^{rx}$. Porosity evolution follows mass balance within the REV. If porosity is uniform in space and all pore space is fluid accessible then, by definition,

$$\phi \equiv 1 - \frac{V_g^T + R}{V}, \qquad (31)$$

where V_g^T is cumulative grain volume in the REV and R is the source/sink reaction term accounting for mass loss due to dissolution at granular contacts and precipitation in the open pore space. Total granular volume is $V_g^T = V_0(1 - \phi_0)$, while REV volume V evolves in time through volume strain, $V = V_0(1 - \varepsilon_v)$. Therefore,

$$\phi = 1 - \left[\frac{1 - \phi_0}{1 - \varepsilon_v} + \frac{R}{V_0(1 - \varepsilon_v)}\right], \qquad (32)$$

(see also [*He et al.*, 2002]) with reaction volume given by the time summation,

$$R = V_m \sum_t \left(\Delta m_i^{SiO_2} + \Delta m_p^{SiO_2}\right), \qquad (33)$$

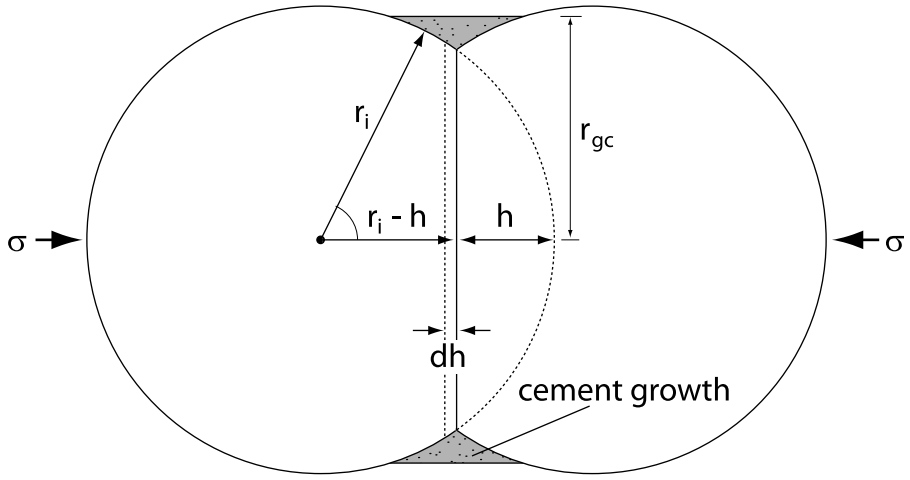

Figure 3. Diagram of compaction and relationship between granular and growing cement radius.

where both $\Delta m_i^{SiO_2}$ and $\Delta m_p^{SiO_2}$ were defined above as positive for dissolution. V_0 is defined as unity, although a good check against geometric construction is that an alternate value for V_0 does not alter simulation results. In a completely closed system, $R \rightarrow 0$ such that no mass is removed from the system but is only redistributed.

[23] Contact area between two interpenetrating spherical particles is given by

$$a_g = \pi h(2r_i - h). \tag{34}$$

We assume a granular material of loose random packing, a more likely scenario than cubic or orthorhombic packing that exhibits approximately $N_c = 6$ contacts per grain and an initial porosity near 40% [*Stephenson et al.*, 1992]. The contact area ratio is therefore given by

$$R_c = \frac{N_c a_g}{S_{ag}}, \tag{35}$$

where S_{ag} is the initial surface area for each particle of mean radius, r_i. Other necessary quantities are specified in Table 1. An assumption of cubic packing is not required. This concludes the derivation of our implicit rate model.

5. Equilibrium Compaction

[24] Constitutive models of pressure solution that utilize equation (11) are ill equipped to handle long-term (complete compaction) analyses. While equation (10) is better positioned for this purpose, significant problems remain. The problem arises from a thermodynamic framework that predicts continued pressure solution until the stress state in the solid matches that of the hydrostat. This, of course, is unlikely and will almost certainly be usurped by the attainment of zero porosity: from observations an apparently unlikely event. Examination of equation (1) shows that the only preventative barrier to this occurrence is the surface energy, U_S.

[25] However, for nominally flat contacts in a purely thin film model, surface curvature $H = 0$, so that surface energy, $U_S = 2H\gamma_G$, is identically zero. If surface roughness exists within the contacts, such as for an island and channel model, potentially reasonable values for surface energy are able to reproduce observed compaction magnitudes provided

Table 1. Experimental Conditions

	σ' [a] (MPa)	T[a] (°C)	r_i[a] (μm)	ϕ_{c-p}[a] (%)	K_b [b] (GPa)	ϕ_0 [c] (%)	R_c [c,d] (%)
qc212[e]	22	503	10	35.41	1.3	36.50	1.7
qc204[e]	51	410	10	38.16	1.3	40.59	3.9
qc213[e]	52	502	10	36.55	2.5	37.87	2.1
qc203[e]	52	506	10	35.58	1.4	37.97	3.7
qc05[e]	100	489	129.1	29.56	1.3	34.98	7.8
qc07[e]	100	489	3.1	41.09	1.3	46.98	10.2
cpf5[f]	50	500	20.5	26.12	0.7	31.80	7.8
cpf6[f]	100	400	20.5	25.14	0.9	33.46	11.3
cpf3[f]	100	500	23.5	27.31	1.3	33.13	8.1
cpf8[f]	100	500	15.5	31.08	1.4	34.07	7.2
cpf7[f]	100	600	21.6	31.38	1.5	35.96	6.7
cpf4[f]	150	500	21.5	29.39	1.7	29.39	9.0

[a]As reported in the original work.
[b]Assigned in this work.
[c]Calculated.
[d]Initial contact area ratio (at ϕ_{c-p}).
[e]Experiment of *van Noort et al.* [2008a].
[f]Experiment of *Niemeijer et al.* [2002].

average grain boundary separation is sufficiently thin (~5nm) [i.e., *van Noort et al.*, 2008b]. *Heidug* [1991, 1995] showed that surface energy is dependent on (evolving) tangential forces along the contact so that hydrostatically determined values for surface tension may be underestimating the retarding effect of surface energy. Alternatively, grain boundary healing and diffusive resistance from precipitated material at the periphery of grain contacts may have significant retarding effects.

[26] The approach of *Stephenson et al.* [1992] and subsequent applications [*Revil*, 1999, 2001; *Yasuhara et al.*, 2003] was to introduce a "critical stress" that represents some final energy barrier to interpenetration. The phenomenological construction of *Stephenson et al.* [1992] represents the total energy expended (which they referred to as "molar displacement work") over the complete life cycle of an interpenetration event in comparison to the amount of material deposited as cement around an interpenetrating grain. Equilibrium occurs at a predefined value of the burial constant, β_c, representing the relationship between total granular interpenetration, h, and the radial extent of deposited "supporting" cement, r_{gc},

$$\beta_c = \frac{r_{gc}/r_i}{1 - h/r_i} \tag{36}$$

with both values referenced to the initial granular radius, r_i (Figure 3). The equilibrium value of stress when this is achieved is $\sigma_a^{eq} = \sigma_c \beta_c^2$, where σ_c is the critical stress. Hence, equilibrium is obtained when

$$\sigma_a \rightarrow \sigma_a^{eq} = \frac{E_A(1 - T/T_A)N_c(1 - \phi_0)}{4V_m}\beta_c^2, \tag{37}$$

where T_A is approximated as the melting temperature and E_A is approximated by the molar heat of fusion, for $N_c \approx 6$ contacts per grain, and the initial porosity, ϕ_0. This result differs from the adaptation of *Revil* [1999] and *Yasuhara et al.* [2003] by maintaining the dependence on porosity, contacts per grain, and importantly, β_c. See *Stephenson et al.* [1992] for the derivation of these parameters and a discussion of the terms T_A and E_A. Note that equation (37) is derived from a granular media geometry [see *Stephenson et al.*, 1992] and that single contact predictions (as in rough fractures) will differ in geometric factor.

[27] This approach (of *Stephenson et al.* [1992]) is novel in that it does not follow the form of equation (1), $\Delta\mu = \sigma_a V_m + \Delta f - 2H\gamma_G$, which is a statement of local, incremental equilibrium (see for example, *Lehner* [1995]) but is a statement of the total energy expended over a pressure solution life cycle, indexed to a final energy barrier, β_c. Therefore, β_c is a total energy formulation for healing at the grain periphery, resulting in increased contact area (support) and, potentially, diffusive blockage. It may be of interest to examine the brief discussion in the study of *Lehner* [1995] regarding the "problem of Stefan" (*Carslaw and Jaeger* [1959], chapter 12), which relates strongly to the pressure solution mechanism and to the formulation presented by *Stephenson et al.* [1992]. To represent this final equilibrium, *Yasuhara et al.* [2003] suggests

$$\Delta\mu = \frac{(\sigma_a - \sigma_a^{eq})}{\alpha} V_m \tag{38}$$

as a modified form of equation (1), where σ_a^{eq} includes the contribution from (positive) Helmholtz and (negative) surface energy at final compaction. It is apparent from this discussion that σ_a^{eq} should also represent energy contribution from the supporting cement, a contribution that is otherwise absent from equation (1). Inserting equation (38) into equation (11),

$$\dot{m}_i^{rx} = k^+ A_i^{rx} \frac{(\sigma_a - \sigma_a^{eq})V_m}{RT}. \tag{39}$$

This result (equation (39)), first derived in the study of *Revil* [1999], allows dissolution to attain a final equilibrium provided σ_a^{eq} is significant relative to σ_a, the dependence on A_{rx}^i is upheld. Following this approach, we substitute likewise for equation (8),

$$\dot{m}_i^{rx} = k^+ \alpha A_i^{rx} \exp\left(\frac{(\sigma_a - \sigma_a^{eq})V_m}{\alpha RT}\right)\left(1 - \frac{\tilde{C}_i}{C_{eq}^{\sigma}}\right). \tag{40}$$

Note that as long as α is considered to be steady state during compaction, the approximations made on a_{SiO_2} to achieve equation (11) (and thus equation (39)) lead to cancellation of α from the relationship. Therefore, contact fraction α can only be considered in equation (40), where its dependence is exponential.

[28] Note also that the method chosen to represent equilibrium compaction is independent of the implicit rate formalism presented in sections 3–4. Should an alternate representation be chosen to represent chemical potential (see section 10, for instance), it is only required to insert this new chemical potential into equation (8) and proceed as outlined in sections 3–4.

6. Model Comparisons: Influence of Concentration

[29] Figure 4 shows the results of the current model in comparison to alternative derivations. Three alternative models (m1, m2, and m3) are considered. The calculation sequence developed in this paper (Figure 2) is represented by model m1. Model m2 utilizes a simplified parallel dashpot model for the transition from diffusion to dissolution limited regimes and thus utilizes equation (39) rather than equation (40). The molar viscous equations for dissolution and diffusion, respectively, are [cf. *Raj*, 1982; *Revil*, 2001; *Rutter*, 1976],

$$q_{diss} = k^+ \alpha A_i^{rx} \frac{V_m}{RT} \tag{41}$$

$$q_{diff} = 32 D_f \omega \frac{V_m}{RT} C_{eq}^h \tag{42}$$

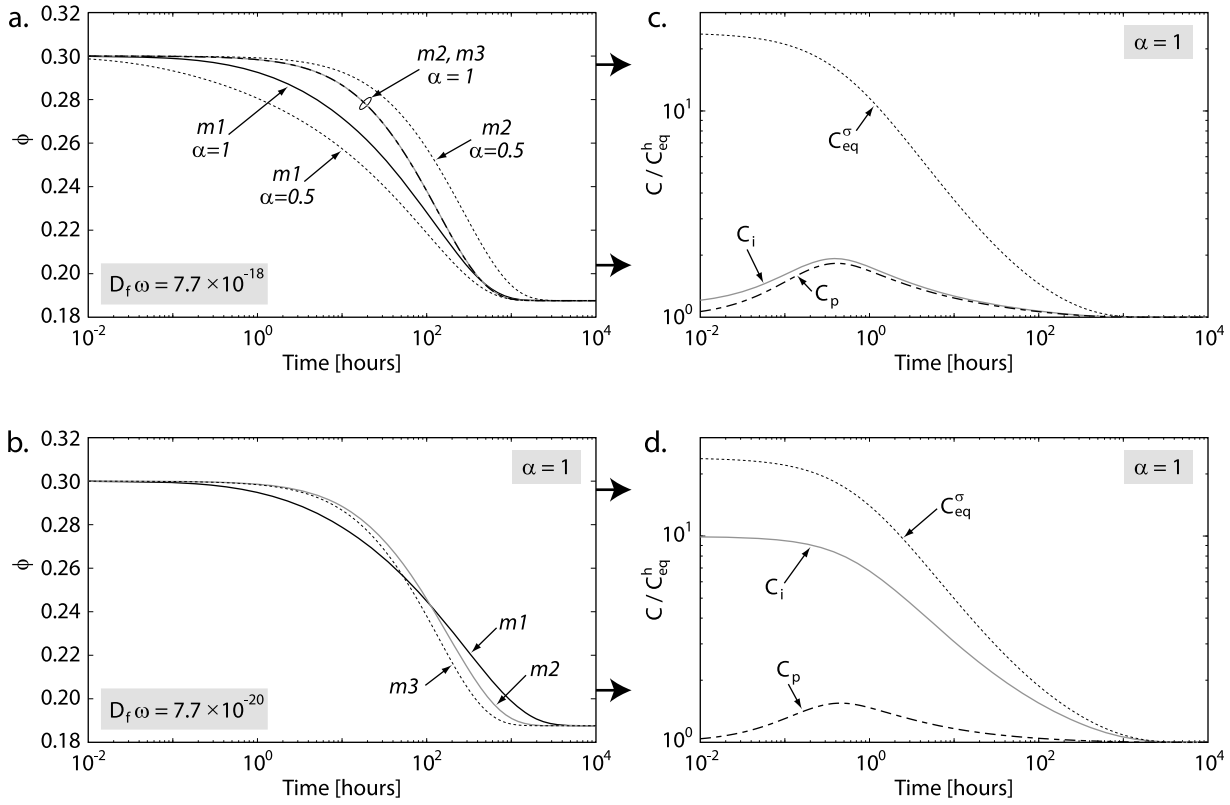

Figure 4. Comparison of alternate models. All cases utilize T = 350°C and $\sigma' = 50$ MPa. Model m1 is the implicit calculation sequence presented in this paper, m2 is the viscous dashpot model, and m3 is equation (39) only. All concentrations normalized to $C_{eq}^{h} = 12.997$ mol/m^3 (350°C). At 350°C, $k^+ = 6.05 \times 10^{-8}$ mol m^{-2} s^{-1}. Simulations utilize a low bulk modulus (1 GPa, see Appendix A), to ensure a higher initial contact area and the absence of early time rate overestimation (section 8.1).

with total viscous behavior given by $1/q_T = 1/q_{diss} + 1/q_{diff}$, and

$$\Delta m_i^{SiO_2} = q_T \frac{(\sigma_a - \sigma_a^{eq})}{\alpha} \Delta t. \quad (43)$$

Equation (41) is a restatement of our equation (11). All variables are as defined above. The factor 32 in the diffusion equation comes from additional thermodynamic considerations on equation (16) [*Rutter*, 1976]. Model m3 uses equation (39) only (does not consider diffusion). The fundamental difference between the models is the use of equation (39) to represent intergranular dissolution in both models m2 and m3 rather than the concentration dependent equation (40) for m1 (with implicit, dissolution-diffusion coupling). Both m2 and m3 are concentration independent and are unable to track pore precipitation. Therefore, pore precipitation has been disabled in m1 for these comparisons. This is equivalent to assuming a fully closed system, where all material dissolved at contacts is simultaneously redistributed to the open pore. Contact fraction α, as discussed in the previous section, cannot be represented in model m3. While the resistive formulation of m2 does allow contribution from α, its behavior will be largely different than for the exponential α dependence in m1.

[30] Figure 4a shows that, as expected, models m2 and m3 are identical when dissolution is dominant. A decrease in diffusivity (Figure 4b) illustrates the difference between m2 and m3. In all cases, it is clear that the regimes are never fully dissolution controlled (in the sense of being concentration independent). Even when dissolution is clearly the dominant mechanism (Figure 4a for instance, where m2 and m3 are identical), the concentration-dependent model, m1, produces different results because interfacial concentration affects the rate of dissolution. The effect of α is also demonstrated in Figure 4a. While m3 is independent of this parameter, m2 and m3 are significantly affected and in fundamentally different ways. The concentration profiles of Figures 4c and 4d (for model m1) show clearly the competition between diffusion and dissolution.

7. Parameter Sensitivity

[31] Parametric analyses reaction rate and diffusivity are provided in Figure 5. The importance of shifts in these parameters is not independent of direction, as decreases in rate constant and diffusivity hold a much stronger sway on compaction than does a corresponding increase. This is indicative of a strongly coupled system, where increases in reaction rates are countered by a diffusive limitation and decreases in diffusivity by dissolution limitation. In fact,

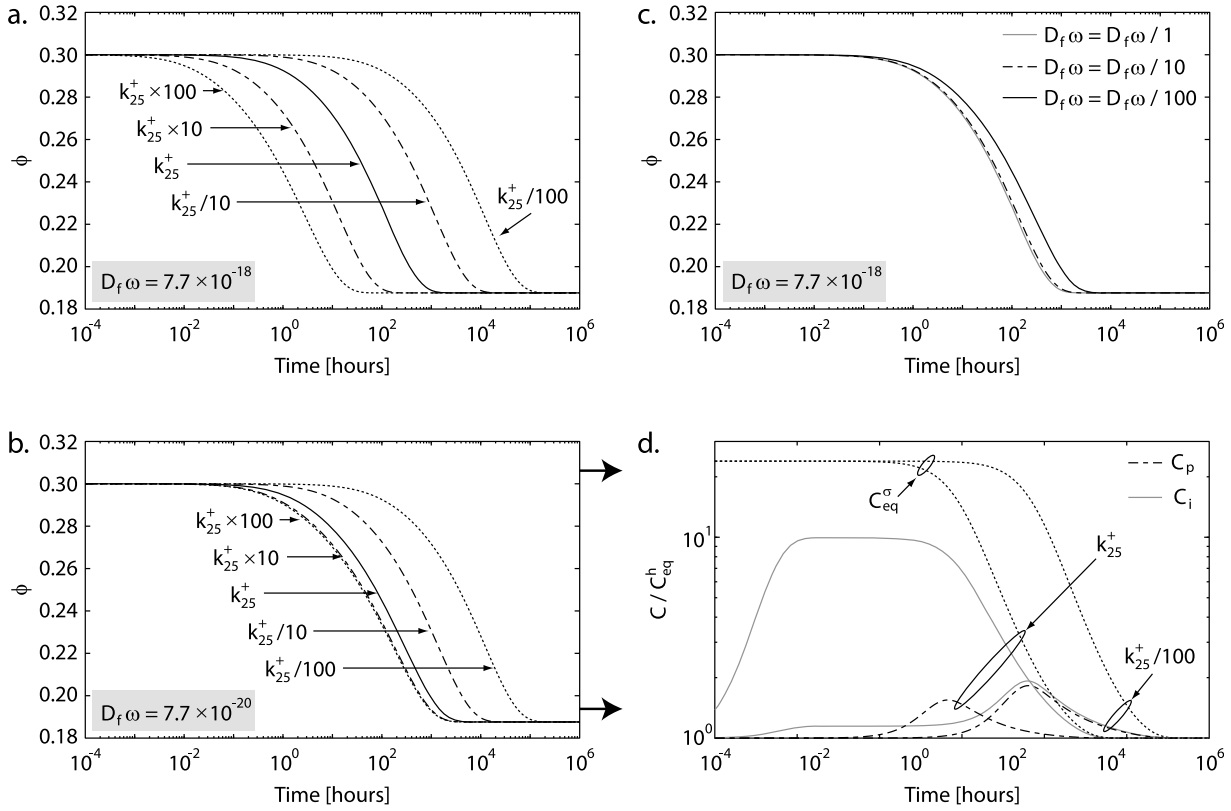

Figure 5. Comparison of various parameter changes with T = 350°C, σ' = 50 MPa, α = 1. All concentrations normalized to C^h_{eq} = 12.997 mol/m^3 (350°C). At 350°C, $k^+ = 6.05 \times 10^{-8}$ mol m^{-2} s^{-1}. Simulations utilize a low bulk modulus (1 GPa, see Appendix A), to ensure a higher initial contact area and the absence of early time rate overestimation (section 8.1).

these figures can largely be viewed as variations in the dissolution/diffusion/precipitation system rather than as an illustration of the importance of any one parameter. Figure 5b decreases the diffusivity (shifting toward diffusive control) and reexamines the behavior of Figure 5a. In this case increases of rate constant have a smaller effect on compaction, as diffusion is now a stronger player.

[32] In this system, order of magnitude changes in diffusivity is required to produce strongly visible changes in compaction rate. With regard to the intergranular film width, ω, much of the literature places this parameter in the range 2–10 nm, and changes of this magnitude have an insignificant effect on compaction. The fractional contact parameter, α, is an important contributor to behavior, as illustrated in Figure 4. The burial constant, β_c, is the primary control on final compaction magnitude, and so the effect of parameter variation is to alter the final porosity. Methods to obtain it and a discussion of its characteristics are found in the following section and Appendix A.

8. Experimental Comparisons

[33] This section introduces predictive comparisons of our model against the laboratory results of *Niemeijer et al.* [2002] and *van Noort et al.* [2008a]. In these experiments, both the initial and final porosity are known, so that the burial constant may be directly calculated (Appendix A). We find, in agreement with *Niemeijer et al.* [2002], that behavior is indeed dissolution dominated under these experimental conditions. Changes to diffusivity, at least within 1–2 orders of magnitude, have only minor (if any) effects on compaction rate. Experimental conditions of the various curves in Figures 6–8 are shown in Table 2.

[34] Figure 6 compares model results to the experiments of *van Noort et al.* [2008a]. The zero stress porosity, ϕ_0, is

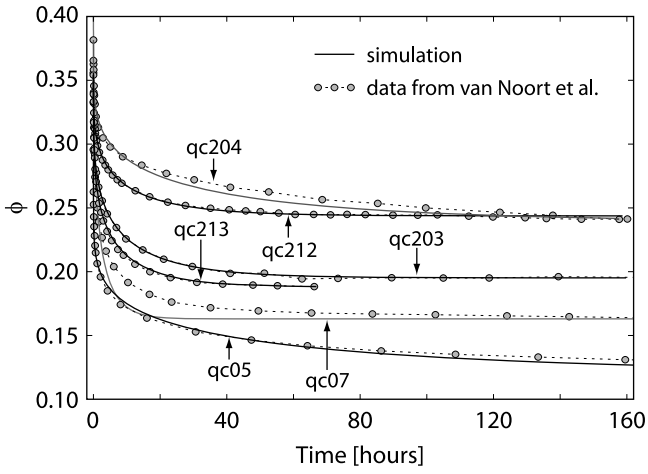

Figure 6. Comparison of model with data from *van Noort et al.* [2008a]. Experimental conditions in Table 2.

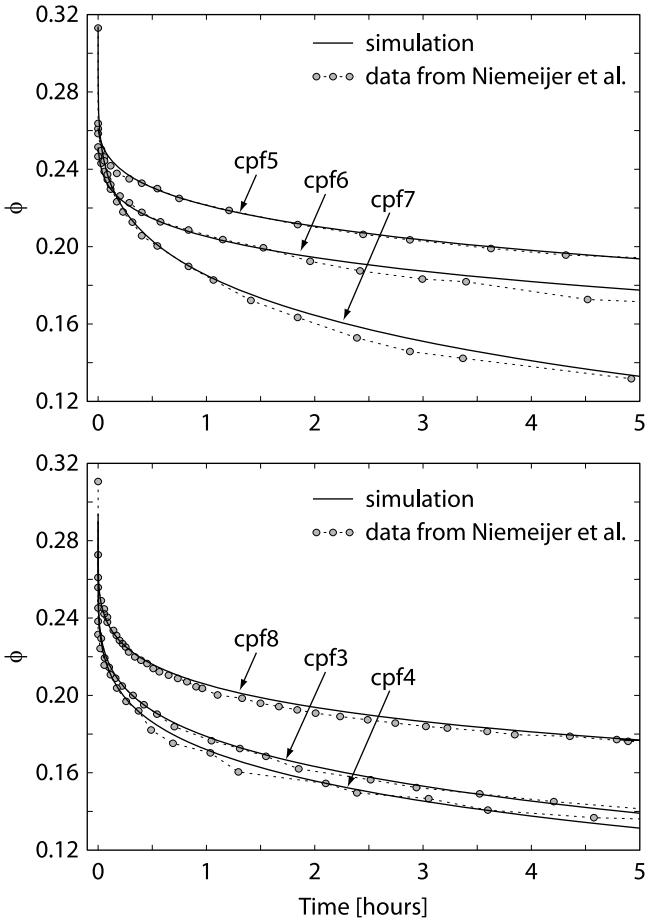

Figure 7. Comparison of model with data from *Niemeijer et al.* [2002]. Experimental conditions in Table 2.

calculated according to section A1 and then β_c according to section A2. Between experiments, only the bulk modulus, K_b, of the composite sample (used to obtain ϕ_0) is varied; all others are held constant. Such variations are conceptually reasonable, given differences in grain arrangements between samples (and potentially grain size). The variation, however, is quite small, averaging 1.3 GPa and ranging from about 1 to 2 GPa (somewhat smaller than typical values of ~8 GPa for Berea sandstone, for instance). Because this value determines the initial contact area ratio in the compressed samples, the smaller value is likely accommodating for imperfections from the spherical particle approximation. The result is that initial contact area ratio is stress dependent, varying from 3% to 4% at 50 MPa to 7% to 8% at 100 MPa effective stress and shifting slightly between samples. The least accurate match occurs for sample qc07, which exhibits by far the smallest particle size, and for which the compaction rate is overestimated throughout the experiment. Particle size variations between other experiments do not appear to cause problems.

[35] Figure 7 takes a larger step and compares the same model to the experimental results of *Niemeijer et al.* [2002]. In many of these experiments, the true final porosity is not known because of sudden cessation of compaction that could not be explained and appears to be noncongruent with a natural process. They suggested that chemical interference from the testing materials might have altered the dissolution process. This characteristic behavior shares very similar form to several of the results from *van Noort et al.* [2008a] that resulted from precipitated silica blockage of the output fluid lines. Therefore, βc is adopted, as a function of stress only, from the results of *van Noort et al.* [2008a] where necessary. Figure 7 shows only the initial data of *Niemeijer et al.* [2002] for visualization purposes. Figure 8 shows model data in comparison to the full time data of *Niemeijer et al.* [2002]. As before, no parameter adjustments are made between experiments aside from slight adjustments to the initial porosity, via K_b.

8.1. Overestimation of Compaction Rates

[36] Plotting these same results versus log(*time*) shows that for all data from *van Noort et al.* [2008a], compaction rates in early times (approximately <15 min) are consistently overestimated (Figure 9). The time of overestimation increases proportionally with stress. This same phenomenon has been noted elsewhere (for example, *van Noort et al.* [2009]) and is intuitively explained. During this time, contact area ratio within the samples is generally <5%–8% (Table 2, and see *Karcz et al.* [2008] and *van Noort et al.* 2009]), leading to disjoining stresses in excess of plastic flow criteria. If this process is rate limiting in comparison to higher compaction rates from dissolution, then compaction would be slowed to the plastic flow rate and the energy contribution to chemical potential (equation (1)) dissipated. If this, or some other, process is not rate limiting, then dissolution rates will be markedly enhanced (Figure 9), along with predicted interfacial concentrations (by equations (1), (8), and (10)).

[37] This can be examined (for illustrative purposes only) by introducing a mechanical buffer to the pressure solution model. The mechanical buffer curve in Figure 9 is obtained by placing a stress cap on the model. Disjoining stress is restricted to this maximum value (representing the stress above which plastic flow would dominate). While mechanistically only an approximation, the result illustrates that such an energy limitation could potentially explain the early rate overestimation, without altering the behavior of pressure solution in later times.

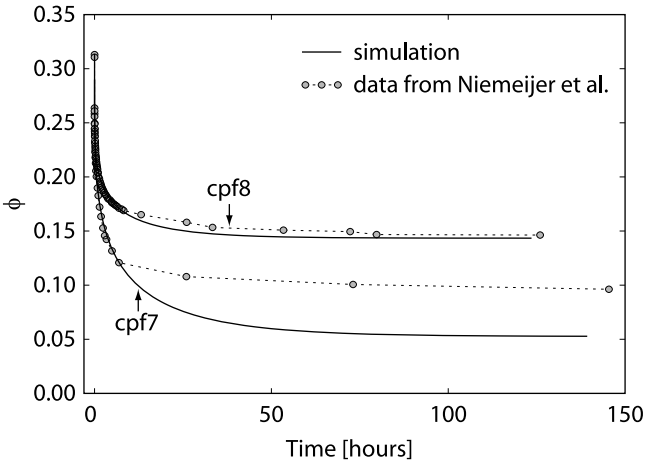

Figure 8. Full time comparison to the data of *Niemeijer et al.* [2002]. Experimental conditions in Table 2.

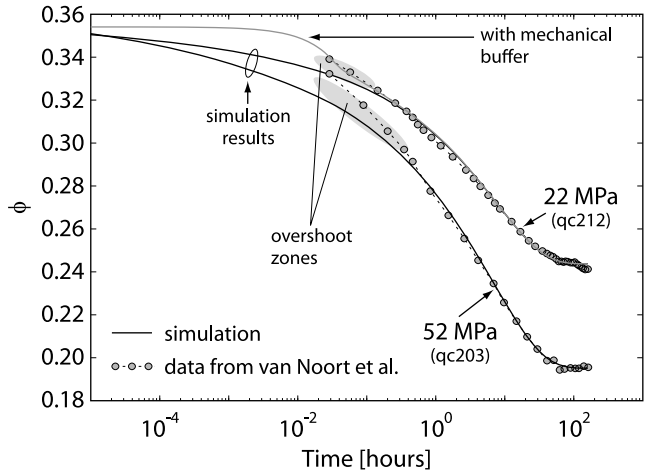

Figure 9. Compaction overestimation in early times. "Mechanical buffer" curve places a stress cap on chemical potential (see text).

[38] This overestimation, however, is not present in most of the data of *Niemeijer et al.* [2002]. Note (Table 2) that ϕ_{c-p} is consistently lower for these experiments compared to the data from *van Noort et al.* [2008a] at similar stress, which may indicate the prior contribution of some additional compaction process. The reasons for this, however, are unclear.

8.2. Stress Dependence and the Burial Constant

[39] Results of the previous section indicate that effective stress is an important contributor to equilibrium compaction, referenced by the fact that β_c appears largely to be a function of stress alone (Figure 10). Temperature effects appear to be accommodated correctly, at least approximately, by the remaining portion of the critical stress. Simulations were also conducted (utilizing the above formation, and see section 10) utilizing surface energy (equation (2)) and strain energy (equation (3)) to control final equilibrium (without critical stress). It is possible with this method to reproduce final compaction for individual experiments with adjustment of surface energy parameters. However, the lack of stress dependency in the simplified formulation of equation (2) prohibits the possibility of extension to arbitrary conditions of stress. Stress-dependent surface energy, or the inclusion of some other stress dependent process, would be required to extend the model to arbitrary stress conditions. In the current formulation, only the stress-dependent burial constant is capable of this.

9. Natural Data

[40] Utilizing the burial constant data from Figure 10, it is possible to make an extension of final compaction magnitudes to naturally observed data. This is conducted in Figure 11. Data for Figure 11 come from *Ramm* [1992], and initial porosity is obtained by following the relationship for grain compression and reorientation proposed therein. The relationship proposed there is $\phi_{c-p} = 45\exp(-\eta Z)$, where $\eta = \ln(2)/Z_{1/2}$, where Z is depth (km) and $Z_{1/2}$ is defined as the "half-porosity depth," or the depth at which half of the mechanically reduced porosity is obtained. ϕ_0 is then given according to section A1. Burial constant is taken directly as the polynomial fit of Figure 10, with K_b taken as the average from experiments, 1.3 GPa, for lithostatic (effective) stress of 12.1 MPa/km and a geothermal gradient of 35°C/km [*Ramm*, 1992].

10. Diffusion Control Through a Cement Sheath

[41] An alternate method to obtain equilibrium is to exclude the critical stress and rely solely on grain periphery healing to rate control a final equilibrium. This rate-controlled process progressively decreases the disjoining stress by adding to granular contact area (affects the $\sigma_a V_m$ term) and increases diffusive resistance around the grain. In this case the full form of equation (1) is used, with strain energy provided by equation (3) and surface energy by equation (2). Methods for

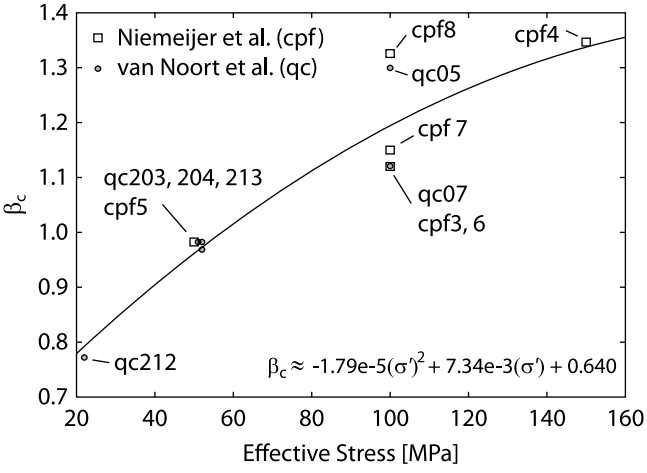

Figure 10. Burial constant results from simulated experiments of *Niemeijer et al.* [2002] and *van Noort et al.* [2008a].

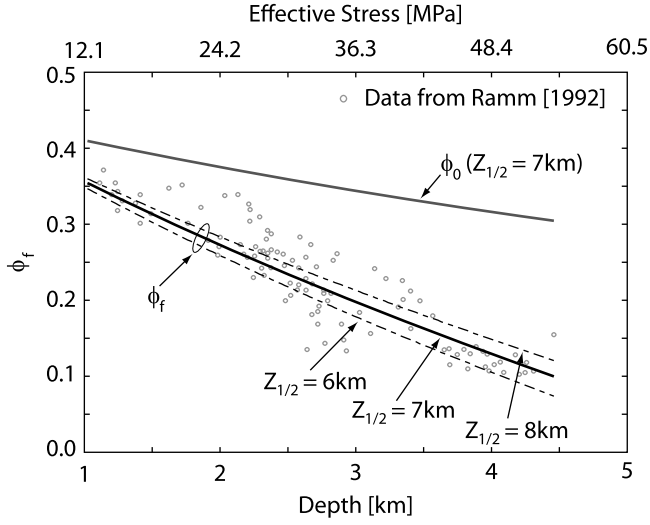

Figure 11. Comparison to natural data of *Ramm* [1992]. Lithostat: 12.1 MPa/km. Geotherm: 35°C/km.

approximating surface energy are, for instance, given by *van Noort et al.* [2008b].

[42] It is possible to examine this by extending the above mass balance system with a second finite element. With reference to Figure 1 (two-element conceptualization), the new system comprises three nodes, the first representing the intergranular contact area, a second node in the pore space immediately surrounding the grain periphery, and a third node in the open pore space. Diffusion from the intergranular contact enters the grain periphery region through the first finite element and then bulk diffusion (represented by the bulk diffusivity, D_p) allows flux of this material in the open pore. If D_p is small compared to the pore precipitation rate constant, material will deposit more rapidly around the grain. Deposited cement increases the granular contact area and decreases the rates of diffusion and dissolution. The mathematical development of this system is presented in Appendix B. Discussed here are a few brief conclusions from this analysis.

[43] Diffusion limitation from a growing neck is sufficient to significantly inhibit compaction, but the trend of the data utilizing this method does not agree with experimental results. Several of the experiments may be accurately fit with this method but not in a way that is extensible to alternate conditions.

[44] The cement region is assumed to behave differently than discrete contacting grains, in that it does not possess a thin film and so does not undergo dissolution precipitation creep (equation (B9)). Rate reductions from this simple approximation, however, do not appear to account fully for dissolution restriction caused by a cement neck. Because the area of cement in contact is, in these analyses, actually quite small (see also the figures in the study of *Niemeijer et al.* [2002] and *van Noort et al.* [2008a]), very little rate limitation occurs.

[45] Because of its limiting dissolution rate, cement will "support" the granular contact as a function of its area of contact and the mechanical constants of the grain and cement. This seems the more likely scenario that could lead to equilibrium compaction and is in line with the results above (stress dependent burial constant). A more complex analysis incorporating stress effects into the achievement of cement driven equilibrium would be required to examine this potential.

11. Discussion

[46] A fully implicit model was developed for the serial processes of dissolution/diffusion/precipitation during the process of dissolution precipitation creep. Maintaining a concentration-dependent dissolution flux introduces important restrictions on rate behavior. Compared to an implicit model, concentration-independent methods appear to appropriately represent a mean compaction behavior, slightly underestimating rates in dissolution-dominated regimes and slightly overestimating in diffusion limitation. Aqueous concentration in the intergranular film affects dissolution rate at all times so that the rate of diffusive flux can influence compaction rates, even in "dissolution-limited" regimes.

[47] The use of a modified critical stress is capable of reproducing final pressure solution equilibrium with reasonable accuracy. Any reasonable method may however be chosen to represent the decline in chemical potential and thus compaction equilibrium. The resulting chemical potential need only be inserted into the implicit rate model (via equation (8)). While it seems unlikely that any single pressure solution model will be applicable to all scenarios, the combined model presented here reproduces experimental data with reasonable accuracy across a range of experimental conditions, suggesting that the concept applied to the model may be progressing in the correct direction.

[48] Reproducing equilibrium compaction with rate-controlled cement deposition is not possible with the simplified model presented here in all but rare cases. Therefore, it is not yet clear what precise mechanism is being compensated for by the use of a burial constant. The argument presented in the previous section regarding the development of a nonreactive (or at least not stress activated) mechanical support frame developed from deposited silica seems reasonable given the derivation of the burial constant (derived with exactly this purpose [*Stephenson et al.*, 1992]), further supported by its dependence on effective stress. However, other processes cannot be ruled out, such as the eventual decay in stress levels below the compressive strength of nonuniform granular contacts. In either case, further mechanical considerations may be capable of defining final compaction, whether or not this includes contribution from a growing cement neck around the grain periphery.

Appendix A

A1. Initial Porosity

[49] *Niemeijer et al.* [2002] and *van Noort et al.* [2008a] followed a similar experimental procedure. Samples were first cold pressed at the desired experimental stress to allow for mechanical compression and grain reorientation. Hydrothermal pressure solution compaction monitoring began from this stage of initial porosity, which we will call ϕ_{c-p} (for cold pressed). The porosity referred to in this paper as ϕ_0, is the zero-stress porosity following grain reorientation. It is, therefore, ϕ_{c-p} decompressed (through elastic expansion, not reorientation) to a value of zero stress. For perfectly spherical particles, it is this value, ϕ_0, where contact area between grains is approximately zero, and it is from this value that *Rutter* [1983] defines a contact area relationship of $R_c = (\phi_0 - \phi)/\phi_0$ and where we assume that contact interpenetration is approximately zero. A bulk modulus of the bulk material (in the "drained," or long-term limit) is used to relate ϕ_0 and ϕ_{c-p}

$$\varepsilon_v = \sigma'/K_b \tag{A1}$$

$$\phi_{c-p} = 1 - \frac{1-\phi_0}{1-\varepsilon_v}. \tag{A2}$$

This assigns the initial mechanical strain, mechanical interpenetration, and contact area ratio at ϕ_{c-p}, where the experiments begin. Once ϕ_0 is known, β_c may be calculated according to the following section.

A2. Direct Calculation of Burial Constant

[50] In these experimental comparisons, both the initial and final porosity is approximately known. In this case the

burial constant may be directly calculated. Assuming a fully closed system, from equation (32), the volume strain at final compaction is $\varepsilon_v^f = (\phi_0 - \phi_f)/(1 - \phi_f)$. With the linear strain provided by equation (30) as $\varepsilon_l^f = 1 - (1 - \varepsilon_v^f)^{1/3}$. Substituting equation (34) into equation (35) and substituting the quantity, $h = \varepsilon_l^f r_i$, into the result yields

$$R_c = \frac{N_c \varepsilon_l^f \left(2 - \varepsilon_l^f\right)}{4} \tag{A3}$$

for the contact area ratio at final compaction. From equation (37), and given $\sigma_a = \sigma'/R_c$, the burial constant is

$$\beta_c = \sqrt{\frac{\sigma'}{R_c \sigma_c}} \tag{A4}$$

with R_c given by equation (A3) and with

$$\sigma_c = \frac{E_A(1 - T/T_A)N_c(1 - \phi_0)}{4V_m}. \tag{A5}$$

Accuracy of this result depends on the degree of closure in the system. In a completely closed system, mass loss $\rightarrow 0$, the result is quite accurate.

Appendix B

B1. Composite Mass Balance

[51] To better capture behavior in the neck growth area, a reasonable extension is to include a second element in the finite element system. With reference to Figure 1 (two-element conceptualization), the new system comprises three nodes: the first representing the intergranular contact area, a second node in the pore space immediately surrounding the grain periphery, and a third node in the open pore space. Diffusion from the intergranular contact enters this region through the first finite element, and then bulk diffusion (represented by the bulk diffusivity, D_p) allows flux of this material in the open pore. If D_p is small compared to the pore precipitation rate constant, material will deposit more rapidly around the grain. For two elements, we require four mass balance equations: the first two representing the relationship between the contact area and grain periphery (subscripted c for cement),

$$\dot{C}_i V_i = k^+ A_i^{rx} a_{SiO_2} \left(1 - \frac{\tilde{C}_i}{a_{SiO_2} C_{eq}^h}\right) - D\left(\tilde{C}_i - \tilde{C}_c\right) \tag{B1}$$

$$\dot{C}_c \frac{V_c}{2} = k^+ \frac{A_c^{rx}}{2} \left(1 - \frac{\tilde{C}_c}{C_{eq}^h}\right) + D\left(\tilde{C}_i - \tilde{C}_c\right) \tag{B2}$$

where the volume of the cement region, V_c, is divided equally between each element (divide by 2), D is diffusivity in the intergranular space (equation (21)), and A_c^{rx} is reactive area within the cement region. The second mass balance system represents precipitation and bulk diffusion from the cement region to open pore,

$$\dot{C}_c \frac{V_c}{2} = k^+ \frac{A_c^{rx}}{2} \left(1 - \frac{\tilde{C}_c}{C_{eq}^h}\right) - D_p\left(\tilde{C}_c - \tilde{C}_p\right) \tag{B3}$$

$$\dot{C}_p V_p = k^+ A_p^{rx} \left(1 - \frac{\tilde{C}_p}{C_{eq}^h}\right) + D_p\left(\tilde{C}_c - \tilde{C}_p\right) \tag{B4}$$

In this system, D_p is bulk diffusivity in the open pore. Distributing these four relationships into local matrices, as in equation (22), and adding the system leads to the global linear system,

$$\begin{Bmatrix} k^+ A_i^{rx} a_{SiO_2} \\ k^+ A_c^{rx} \\ k^+ A_p^{rx} \end{Bmatrix} = \begin{bmatrix} V_i & 0 & 0 \\ 0 & V_c & 0 \\ 0 & 0 & V_p \end{bmatrix} \begin{Bmatrix} \dot{C}_i \\ \dot{C}_c \\ \dot{C}_p \end{Bmatrix}$$

$$+ \begin{bmatrix} \left(\frac{k^+ A_i^{rx}}{C_{eq}^h} + D_i\right) & -D_i & 0 \\ -D_i & \left(\frac{k^+ A_c^{rx}}{C_{eq}^h} + D_i + D_p\right) & -D_p \\ 0 & -D_p & \left(\frac{k^+ A_p^{rx}}{C_{eq}^h} + D_p\right) \end{bmatrix} \begin{Bmatrix} C_i \\ C_c \\ C_p \end{Bmatrix} \tag{B5}$$

with the global implicit solution,

$$\begin{Bmatrix} C_i \\ C_c \\ C_p \end{Bmatrix}_{t+\Delta t} = \begin{bmatrix} \left\{\left(\frac{k^+ A_i^{rx}}{C_{eq}^h} + D_i\right) + \frac{V_i}{\Delta t}\right\} & \{-D_i\} & \{0\} \\ \{-D_i\} & \left\{\left(\frac{k^+ A_c^{rx}}{C_{eq}^h} + D_i + D_p\right) + \frac{V_c}{\Delta t}\right\} & \{-D_p\} \\ \{0\} & \{-D_p\} & \left\{\left(\frac{k^+ A_p^{rx}}{D C_{eq}^h} + 1\right) + \frac{V_p}{\Delta t}\right\} \end{bmatrix}_t^{-1} \times \begin{Bmatrix} k^+ A_i^{rx} a_{SiO_2} + \frac{V_i C_i}{\Delta t} \\ k^+ A_c^{rx} + \frac{V_c C_c}{\Delta t} \\ k^+ A_p^{rx} + \frac{V_p C_p}{\Delta t} \end{Bmatrix}_t \tag{B6}$$

B2. Cement Characteristics

[52] As a cement neck grows from the grain contact the total (grain + cement), contact area of a single contact is calculated from (assuming uniform deposition around the grain contact)

$$a_{gc} = \pi(h + c_d)(2r_i + c_d - h) \tag{B7}$$

for the depth (orthogonal to grain surface) of deposited cement, c_d, and the granular interpenetration, h. Contact area due only to the granular contact (excluding cement) is given by equation (34). The disjoining stress is now a function of the total contact area calculated from a_{gc} rather than a_g as above. While molecular diffusion should not differ significantly within the cement neck, the tortuosity of such a layer is potentially large. Uniform deposition around the grain periphery could lead to significant diffusive resistance, while a nonuniform deposition would have little impact. A number of complicating factors arise in the description of neck growth and only a simple probing analysis is conducted here to examine the potential for diffusion or rate limitation from such a neck to encourage equilibrium. It is assumed that the neck is uniform and exhibits a large diffusive tortuosity. Diffusive flux through the cement region is then

$$\dot{m}^{diff} = \frac{2\pi D_f \omega}{\tau_f^c \ln(r_{gc}/r_g)}\left(\tilde{C}_i - \tilde{C}_c\right) \tag{B8}$$

(*Carslaw and Jaeger* [1959]; section 7.2.I), where r_{gc} is total (grain + cement) contact radius (see Figure 1), r_g is grain-only contact radius, $\tilde{C}_c$ is concentration in the cement region, and τ_f^c is the diffusive tortuosity factor for the neck region. Total intergranular diffusion is then given by the limiting behavior of either equation (B8) or of granular diffusion given by equation (17). Equation (B8) will grow larger with the ratio of cement radius to grain radius.

[53] Cement will have at least two other effects, both originating in the rate of dissolution from cement contacts. While dissolution would occur at cement edges, there is no experimental or conceptual support for thin film-type diffusion within the cement layer. The first effect then, is that the fraction of contact because of cement will not undergo stress-activated dissolution in any significant magnitude. Second, because of its limiting dissolution rate, cement will "support" the granular contact as a function of its area of contact and the mechanical constants of the grain and cement. This is the more likely scenario that could lead to equilibrium compaction and is in line with the results above (stress-dependent burial constant), but its inclusion requires mechanical analyses beyond the scope of this work. To examine the first effect, we introduce the simple approximation,

$$\frac{1}{a_{SiO_2} k_i^+} = \frac{f_a^c}{k_i^+} + \frac{f_a^g}{a_{SiO_2} k_i^+}, \tag{B9}$$

for the fraction of total contact area due to cement, f_a^c, and grain, f_a^g. This simply states that reaction rate within the cement is not stress activated and treats the dissolution compaction of each region as a resistor in series. Preferential deposition to the cement periphery (prior to bulk diffusion into the open pore) may be accommodated by decreasing bulk diffusivity accordingly.

Nomenclature

a_g	Contact area - single granular interface (equation (34))
a_{SiO_2}	Activity of solid silica (equation (8))
$a_{H_4SiO_2}$	Activity of aqueous silica
A_T	Total contact area (REV) ($V_0(1 - \phi_0)S_{ag}/V_g$)
A_i^{rx}	Intergranular reactive area (REV) ($V_0(1 - \phi_0)N_c a_g/V_g$)
A_p^{rx}	Pore reactive area (REV) ($A_T - A_i^{rx}$)
$\tilde{C}_{i,p}$	Mean concentration (subscript interface or pore) (mol · m^{-3})
C_{eq}^h	Aqueous solubility - hydrostatic (0.11 mol · m^{-3} @ 25 °C)
C_{eq}^σ	Aqueous solubility - intergranular fluid (mol · m^{-3})
D_f	Molecular diffusivity (m^2 · s^{-1}) (equation (18))
K_b	Bulk modulus (<8 GPa)
h, Δh	Interpenetration distance (cumulative or change)
H	Local solid/fluid interface curvature
k^+	Dissolution rate constant (mol · m^{-2} · s^{-1}) (5.04×10^{-14} mol m^{-2} s^{-1} @ 25°C, E_a = 67.4 kJ/mol)
k^-	Precipitation rate constant (mol · m^{-2} · s^{-1})
K_{eq}	Equilibrium constant
$\dot{m}_{i,p}^x$	Mass rate (mol · s^{-1}) (subscript interface or pore), superscript rx for reaction, diff for diffusion
$\Delta m_{i,p}^{SiO_2}$	Change of aqueous silica over a time step (mol)
N_c	Number of contacts per grain
Q_{ss}	Steady state influx of boundary water (m^3 · s^{-1})
r_i	Initial (time = 0) mean particle radius
R_c	Contact area ratio (equation (35))
S_{ag}	Mean surface area per grain
U_S	Surface energy (J · mol^{-1})
U_E	Elastic strain energy (J · mol^{-1})
U_D	Dislocation energy (J · mol^{-1})
V_m	Molar volume (m^3 · mol^{-1})
V_p	Current total pore volume ($V_0(1 - \varepsilon_v)\phi$)
V_i	Current total interface volume ($A_i^{rx}\omega/2$)
V_g	Mean volume of each grain
V_g^T	Total grain volume (REV) ($V_0(1 - \phi_0)$)

Greek symbols

α	Intergranular roughness (section 3.2)
β_c	Burial constant (section 5)
$\varepsilon_{l,V}$	Strain (subscript linear or volume) (equation (30))
ϕ	Current porosity (transient)
ϕ_{c-p}	Cold-pressed porosity (after mechanical, before hydrothermal)

ϕ_0 Initial (zero-stress) porosity
γ_G Gibbs surface energy ($J \cdot mol^{-1}$)
$\gamma^{h,\sigma}$ Activity coefficient
$\Delta\mu$ Chemical potential gradient ($J \cdot mol^{-1}$)
σ' Effective stress
σ_a Effective disjoining stress
σ_a^{eq} Equilibrium compaction stress ($\sigma_a^{eq} = \sigma_c\beta_c$)
σ_c Critical stress
ω Thickness of intergranular film

[54] **Acknowledgments.** This work is the result of partial support from the US Department of Energy under project DOE-DE-FG36-04GO14289 and from the National Science Foundation under project EAR-0510182. This support is gratefully acknowledged.

References

Atkinson, B. K. (1984), Subcritical crack-growth in geological-materials, *J. Geophys. Res.*, *89*(NB6), 4077–4114.

Bandstra, J. Z., et al. (2008), Appendix: Compilation of Mineral Dissolution Rates, in *Kinetics of Water-Rock Interaction*, edited by S. L. Brantley et al., pp. 737–833, Springer.

Brown, S. R., and C. H. Scholz (1986), Closure of rock joints, *J. Geophys. Res.*, *91*(B5), 4939–4948.

Carslaw, H. S., and J. C. Jaeger (1959), *Conduction of heat in solids*, 2nd ed., 510 pp., Oxford Univ. Press.

Chester, F. M., J. S. Chester, A. K. Kronenberg, and A. Hajash (2007), Subcritical creep compaction of quartz sand at diagenetic conditions: Effects of water and grain size, *J. Geophys. Res.*, *112*, B06203, doi:10.1029/2006JB004317.

Cox, S. F., and M. S. Paterson (1991), Experimental dissolution-precipitation creep in quartz aggregates at high temperatures, *Geophys. Res. Lett.*, *18*(8), 1401–1404.

De Boer, R. B. (1977), On the thermodynamics of pressure solution: Interaction between chemical and mechanical forces, *Geochim. Cosmochim. Acta*, *41*, 249–256.

de Meer, S., et al. (2005), Structure and diffusive properties of fluid-filled grain boundaries: An in-situ study using infrared (micro) spectroscopy, *Earth Planet. Sci. Lett.*, *232*, 403–414.

Dewers, T., and A. Hajash (1995), Rate laws for water-assisted compaction and stress-induced water-rock interaction in sandstones, *J. Geophys. Res.*, *100*(B7), 13,093–13,013, 13,112.

Dewers, T., and P. Ortoleva (1990a), Geochemical self-organization. III: A mechano-chemical model of metamorphic differentiation, *Am. J. Sci.*, *290*, 473–521.

Dewers, T., and P. Ortoleva (1990b), A coupled reaction/transport/mechanical model for intergranular pressure solution, stylolites and differential compaction and cementation in clean sandstones, *Geochim. Cosmochim. Acta*, *54*, 1609–1625.

Dove, P. M. (1995), Geochemical controls on the kinetics of quartz fracture at subcritical tensile stress, *J. Geophys. Res.*, *100*(B11), 22,349–322,359.

Gratier, J.-P., R. Guiguet, F. Renard, L. Jenatton, and D. Bernard (2009), A pressure solution creep law for quartz from indentation experiments, *J. Geophys. Res.*, *114*, B03403, doi:10.1029/2008JB005652.

Gunderson, E., et al. (2002), Coupling between pressure solution creep and diffusive mass transport in porous rocks, *J. Geophys. Res.*, *107*(B11), 2317, doi:10.1029/2001JB000287.

He, W., et al. (2002), A model for porosity evolution during creep compaction of sandstones, *Earth Planet. Sci. Lett.*, *197*, 237–244.

Heidug, W. K. (1991), A thermodynamic analysis of the conditions of equilibrium at nonhydrostatically stressed and curved solid-fluid interfaces, *J. Geophys. Res.*, *96*(B13), 21,909–21,921.

Heidug, W. K. (1995), Intergranular solid-fluid phase transformations under stress: The effect of surface forces, *J. Geophys. Res.*, *100*, 5931–5940.

Jaeger, J. C., et al. (2007), *Fundamentals of Rock Mechanics, Fourth Edition*, 475 pp., Blackwell Publishing, Malden, Mass.

Kamb, W. B. (1959), Theory of preferred crystal orientations developed by crystallization under stress, *J. Geol.*, *67*, 153–170.

Karcz, Z., E. Aharonov, D. Ertas, R. Polizzotti, and C. H. Scholz (2008), Deformation by dissolution and plastic flow of a single crystal sodium chloride indenter: An experimental study under the confocal microscope, *J. Geophys. Res.*, *113*, B04205, doi:10.1029/2006JB004630.

Lehner, F. (1995), A model for intergranular pressure solution in open systems, *Tectonophysics*, *245*, 153–170.

Niemeijer, A. R., et al. (2002), Compaction creep of quartz sand at 400–600C: experimental evidence for dissolution-controlled pressure solution, *Earth Planet. Sci. Lett.*, *195*, 261–275.

Paterson, M. S. (1973), Nonhydrostatic thermodynamics and its geologic applications, *Rev. Geophy.*, *11*, 355–389.

Raj, R. (1982), Creep in polycrystalline aggregates by matter transport through a liquid phase, *J. Geophys. Res.*, *87*, 4731–4739.

Ramm, M. (1992), Porosity-depth trends in reservoir sandstones: theoretical models related to Jurassic sandstones offshore Norway, *Mar. Pet. Geol.*, *9*, 553–567.

Renard, F., et al. (1997), Pressure solution in sandstones: influence of clays and dependence on temperature and stress, *Tectonophysics*, *280*, 257–266.

Renard, F., et al. (1999), An integrated model for transitional pressure solution in sandstones, *Tectonophysics*, *312*, 97–115.

Revil, A. (1999), Pervasive pressure-solution transfer: A poro-visco-plastic model, *Geophys. Res. Lett.*, *26*(2), 255–258.

Revil, A. (2001), Pervasive pressure solution transfer in a quartz sand, *J. Geophys. Res.*, *106*(B5), 8665–8686.

Revil, A., P. Leroy, A. Ghorbani, N. Florsch, and A. R. Niemeijer (2006), Compaction of quartz sands by pressure solution using a cole-cole distribution of relaxation times, *J. Geophys. Res.*, *111*, B09205, doi:10.1029/2005JB004151.

Rimstidt, J. D., and H. L. Barnes (1980), The kinetics of silica-water reactions, *Geochim. Cosmochim. Acta*, *44*, 1683–1699.

Rutter, E. H. (1976), The kinetics of rock deformation by pressure solution, *Phil. Trans. R. Soc. London, Ser. A*, *283*, 203–219.

Rutter, E. H. (1983), Pressure solution in nature, theory and experiment, *J. Geol. Soc. London*, *140*, 725–740.

Schutjens, P. M. T. M. (1991), Experimental compaction of quartz sand at low effective stress and temperature conditions, *J. Geol. Soc. London*, *148*, 527–539.

Schutjens, P. M. T. M., and C. J. Spiers (1999), Intergranular pressure solution in NaCl: Grain-to-grain contact experiments under the optical microscope, *Oil Gas Sci. Technol*, *54*, 729–750.

Shimizu, I. (1995), Kinetics of pressure solution creep in quartz: theoretical considerations, *Tectonophysics*, *245*, 121–134.

Sleep, N. H. (1995), Ductile creep, compaction, and rate and state dependent friction within major fault zones, *J. Geophys. Res.*, *100*(B7), 13,065–13,080.

Stephenson, L. P., et al. (1992), A model for sandstone compaction by grain interpenetration, *J. Sediment. Petrol.*, *62*, 11–22.

Tada, R., and R. Siever (1989), Pressure solution during diagenesis, *Ann. Rev. Earth Planet. Sci.*, *17*, 89–118.

Taron, J., and D. Elsworth (2009), Thermal-hydrologic-mechanical-chemical processes in the evolution of engineered geothermal reservoirs, *Int. J. Rock Mech. Min. Sci.*, *46*, 855–864.

Tenthorey, E., and S. Cox (2006), Cohesive strengthening of fault zones during the interseismic period: An experimental study, *J. Geophys. Res.*, *111*, B09202, doi:10.1029/2005JB004122.

van Noort, R., C. J. Spiers, and G. M. Pennock (2008a), Compaction of granular quartz under hydrothermal conditions: Controlling mechanisms and grain boundary processes, *J. Geophys. Res.*, *113*, B12206, doi:10.1029/2008JB005815.

van Noort, R., et al. (2008b), Influence of grain boundary structure on dissolution controlled pressure solution and retarding effects of grain boundary healing, *J. Geophys. Res.*, *113*, B03201, doi:10.1029/2007JB005223.

van Noort, R., H. J. M. Visser, and C. J. Spiers (2009), Influence of grain boundary structure on dissolution controlled pressure solution and retarding effects of grain boundary healing, *J. Geophys. Res.*, *113*, B03201, doi:10.1029/2007JB005223.

Visser, H. J. M. (1999), Mass transfer processes in crystalline aggregates containing a fluid phase, Ph. D. thesis, 245 pp., Utrecht University, Utrecht.

Walderhaug, O. (1996), Kinetic modeling of quartz cementation and porosity loss in deeply buries sandstone reservoirs, *AAPG Bulletin*, *80*, 731–745.

Weyl, P. K. (1959), Pressure solution and the force of crystallization: A phenomenological theory, *J. Geophys. Res.*, *64*, 2001–2025.

Yasuhara, H., D. Elsworth, and A. Polak (2003), A mechanistic model for compaction of granular aggregates moderated by pressure solution, *J. Geophys. Res.*, *108*(B11), 2530, doi:10.1029/2003JB002536.

Yasuhara, H., D. Elsworth, and A. Polak (2004), Evolution of permeability in a natural fracture: Significant role of pressure solution, *J. Geophys. Res.*, *109*, B03204, doi:10.1029/2003JB002663.

Yasuhara, H., C. Marone, and D. Elsworth (2005), Fault zone restrengthening and frictional healing: The role of pressure solution, *J. Geophys. Res.*, *110*, B06310, doi:10.1029/2004JB003327.

Yasuhara, H., and D. Elsworth (2008), Compaction of a rock fracture moderated by competing roles of stress corrosion and pressure solution, *Pure Appl. Geophys.*, *165*, 1289–1306.

D. Elsworth, College of Earth and Mineral Sciences and Center for Geomechanics, Geofluids, and Geohazards, Penn State University, University Park, PA 16802, USA.

J. Taron, Helmholtz Center for Environmental Research (UFZ), Department of Environmental Informatics, 04318 Leipzig, Germany. (joshua.taron@ufz.de)